Unlocking a Dual-channel Pathway by Single-site Zr in CO_2 Hydrogenation to Methanol

Meng Yang[a,b], Jiafeng Yu[a,c,*], Anna Zimina[c,d,*], Bidyut Bikash Sarma[c,d], Jan-Dierk Grunwaldt[d,c], Ling Zhang[a,b], Hengyong Xu[a], Jian Sun[a,*]

[a]*Dalian Institute of Chemical Physics, Chinese Academy of Sciences, Dalian 116023, Liaoning, China*

[b]*University of Chinese Academy of Sciences, Beijing 100049, China*

[c]*Institute of Catalysis Research and Technology, Karlsruhe Institute of Technology, Hermann-von-Helmholtz-Platz 1, 76344 Eggenstein-Leopoldshafen, Germany*

[d]*Institute for Chemical Technology and Polymer Chemistry, Karlsruhe Institute of Technology, 76131 Engesserstraße 20, Karlsruhe, Germany*

*Corresponding authors. E-mail addresses: yujf@dicp.ac.cn (Jiafeng Yu); anna.zimina@kit.edu (Anna Zimina); sunj@dicp.ac.cn (Jian Sun)

Abstract

Converting CO_2 into methanol on a large scale is of great significance in the sustainable methanol economy. Zirconia are considered to be an essential support in Cu-based catalysts due to its excellent properties on CO_2 adsorption and activation. However, the evolution of Zr species during the reaction and the effect of their structure on the reaction pathways remain unclear. Herein, single-site Zr species in amorphous SiO_2 matrix are created in Cu/ZrO_2-SiO_2 catalysts by means of the strong Zr-Si interaction. *In-situ* X-ray absorption spectroscopy (XAS) reveals that the coordination environment of single-site Zr is sensitive to the atmosphere and reaction conditions. We demonstrate that the CO_2 adsorption is prior on the interface of Cu and single-site Zr, accompanied by the subsequent hydrogenation only following the reverse water-gas-shift (RWGS)+CO-hydro pathway, which is hard to happen on ZrO_2 particles. Thus, it expands a non-competitive parallel pathway as a supplement to the dominant formate pathway, resulting in the enhancement of Cu activity sixfold and twofold based on Cu/SiO_2 and Cu/ZrO_2 catalysts, respectively. The establishment of this dual-channel pathway by single-site Zr species in this work open new horizons for understanding atomically dispersed oxides in catalysis science.

Introduction

The excessive emission of carbon dioxide has constantly contributed to climate change, which has resulted in urgent demands for its utilization. CO_2 hydrogenation to methanol becomes a reliable pathway to reduce the dependence on fossil fuel with the utilization of “green hydrogen” from clean energy and low-cost CO_2 capture technologies[1,2], because methanol is a large-scale transportable liquid energy carrier and a common feedstock for high value-added chemicals[3]. In terms of methanol synthesis *via* CO_2 hydrogenation, it is greatly difficult to make a trade-off between methanol selectivity and CO_2 conversion[4,5]. Thermodynamically, methanol production is favorable at low temperatures due to exothermic reactions, while CO_2 conversion is limited by the poor catalytic activity at those conditions. CO_2 conversion will be enhanced with increasing reaction temperatures, but methanol selectivity dramatically drops at the same time due to the generation of by-product CO from strongly-endothermic reverse water-gas shift reaction (RWGS) at high temperatures[6]. Hence, it is crucial to develop well-performing catalysts with high methanol selectivity without sacrificing CO_2 conversion, thus producing more methanol.

Generally, Cu-based catalysts are considered to be highly active and cost-effective, especially at relatively mild reaction conditions (190-250°C and 2.0-3.0 MPa)[7,8]. Cu-based catalysts display strong support-dependent effects on CO_2 hydrogenation to methanol and follow different reaction mechanisms. For ZrO_2 support, the Lewis acidity[9,10], the strong Cu-Zr interaction[11], the formation of Cu-Zr compounds[12], Cu-ZrO_2 interfacial sites[13,14] have positive roles in CO_2 activation due to the intermediates adsorption and Cu^+ stabilization[15], always following a typical formate pathway[16]. Besides, active species were found to be established in the SiO_2 matrix and exhibited unique properties. From our previous work[17], we revealed that the Cu/SiO_2 catalyst with a slightly distorted Cu–O–Si texture structure derived from a unique shattuckite-like precursor can stabilize abundant Cu^+ species, where Cu^+ could further improve CO* hydrogenation to methanol *via* the RWGS+CO-hydro pathway. Silica support turned cobalt from a nonselective catalyst into highly selective catalyst for methanol production, where the Co–O–SiO_n linkages favored the methanol production *via* *CH_3O intermediates[18]. The isolated Lewis acid Ti^{IV} surface sites on SiO_2 were proposed to stabilize surface intermediates at the metal-support interface[19]. The Cu/SiO_2 catalyst with isolated Zr surface sites exhibited comparable performance and the same reaction pathway with Cu/ZrO_2 catalysts[20]. These results indicated that the coordination environments of active species were essential. Although the identification of active Zn species formed during reaction were well investigated, such as partially reduced ZnO_x[21], CuZn alloy[22,23], and atomically dispersed Zn[24], the structure evolution of active Zr species at practical reaction conditions and their role in reaction pathways remain unclear, especially, those with unique structure and properties need to be further investigated.

In this work, a series of Cu catalysts supported by the combined Zr and Si oxides with different Zr/(Zr+Si) molar ratios (x%) ranging from 0 to 100%, denoted as Cu/ZrSi-x, were synthesized by the one-step flame spray pyrolysis (FSP) method[25,26] that developed decades ago[27] to establish different Zr species *via* strong Zr-Si interactions. The evolution of Cu valence states during reduction and the dynamic variations on Zr species at different reaction conditions were monitored by *in-situ* X-ray absorption spectroscopy (XAS)[28,29]. *In-situ* diffuse reflectance infrared Fourier transform spectroscopy (DRIFTS) was conducted to probe the reaction pathways on different Cu/ZrSi-x catalysts. DFT calculation contributes to understanding the function of different Zr species in the CO_2 adsorption and the regulation of reaction pathways. The synergistic effect of Zr and Si supports compared to Cu/SiO_2 and Cu/ZrO_2 catalysts is discussed concerning catalytic performance, the evolution of active Cu^+ and Zr species, as well as reaction pathways. A dual-channel pathway is unlocked by creating a new active site based on the traditional formate pathway over Cu/Zr-Si catalysts.

Results and discussion

Catalytic performance

Generally, FSP is an appealing single-step method to create a synergistic interplay with a targeted component in nanoparticles, owing to the quenching process from an extremely high temperature[30]. As shown in Figure 1a, all precursors including Cu, Zr and Si were sprayed in the same nozzle in the process of the single-nozzle flame spray pyrolysis (SFSP) method (SFSP-Cu/ZrSi-3). It supplies sufficient contact between Zr and Si oxides and benefits the formation of highly dispersed oxidized Zr species on the SiO_2 with a strong Zr-Si synergy. The high crystallinity of Cu nanoparticles can be confirmed by high-resolution transmission electron microscopy (HRTEM) for all samples studied here (Figure S1). Diffraction spots of Cu can only be detected from the fast Fourier transform (FFT) pattern. The elemental mapping of Cu, Si and O shows clear profiles of the sample in high-angle annular dark field scanning transmission electron microscopy (HAADF-STEM) image except for Zr (Figure S2). For comparison, the contact between Zr and Si oxides was separated by introducing Zr and Si precursors into two different nozzles *via* the double-nozzle flame spray pyrolysis (DFSP) method (DFSP-Cu/ZrSi-3) as described in our previous work[31]. The crystal lattice of ZrO_2 and the corresponding diffraction spots are observed in DFSP sample (Figure S3), and the Zr elemental mapping (Figure S4) exhibits some aggregation of Zr species in contrast to SFSP-Cu/ZrSi-3 sample. These results reveal that Zr species are highly dispersed on the SFSP-made sample, while aggregated ZrO_2 nanoparticles are easily formed due to the lack of dispersant and mix with Cu/SiO_2 particles at the nano level forming a grain-grain heterojunction in the one made by DFSP[32]. The elemental compositions of Cu/ZrSi-3 catalysts made by DFSP and SFSP methods are almost the same (Table S1). The catalytic performance of the SFSP-made sample for CO_2 hydrogenation to methanol reaction is higher than the one made by DFSP (Figure 1b), revealing that the interaction between Zr and Si or the dispersion of Zr species are important for methanol production.

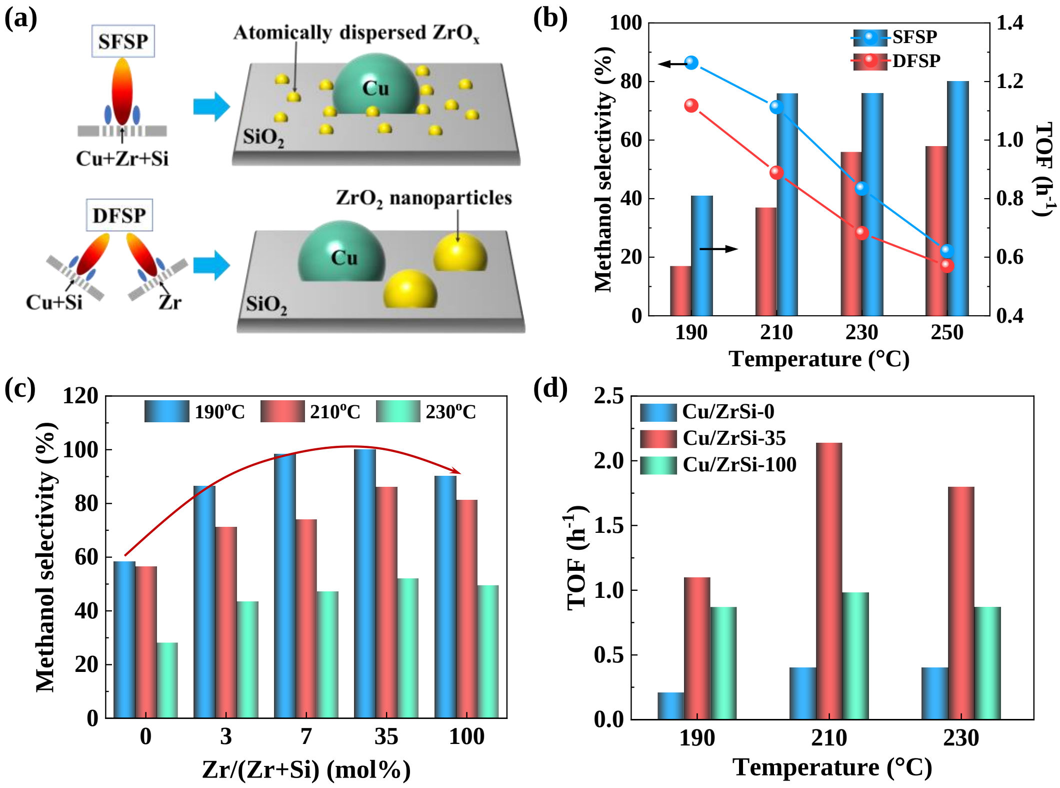

Figure 1. Catalysts and their performance. Establishment of the Zr-Si interaction and the series of Cu/ZrSi-x catalysts: (a) schematic diagram of Cu-Zr-Si catalysts made by SFSP and DFSP methods (SFSP-Cu/ZrSi-3 and DFSP-Cu/ZrSi-3 samples) and (b) their catalytic performance at different temperatures; (c) methanol selectivity as a function of Zr/(Zr+Si) ratio in supports and (d) the turnover frequency (TOF) at various temperatures over CO_2 hydrogenation to methanol reaction. Reaction conditions: 3.0 MPa, H_2:CO_2 = 3:1, GHSV=4000 ml/g_{cat}·h.

Cu/ZrSi ternary catalysts with similar Cu contents but various Zr/(Zr+Si) molar ratios from 0 to 100 % were synthesized by the SFSP method (Table S2). The powder XRD (Figure S5) unravel that ZrO_2 is mainly in tetragonal (t-ZrO_2) rather than monoclinic phase (m-ZrO_2), demonstrating that metastable structure is more readily formed during the quenching process of the FSP preparation method as reported[25]. Strong bands at 1111, 801 and 474 cm^{-1} in FT-IR spectra (Figure S6) that can be assigned to different vibrational modes of Si-O bands further confirm the existence of an amorphous SiO_2 phase[33] in the support. They were stable over several hours and did not show any sign of deactivation at 250 °C (Figure S7). Figure 1c further shows that the addition of a small amount of Zr with a Zr/(Zr+Si) molar ratio of 3% already greatly enhances the methanol synthesis rate compared to the Cu/ZrSi-0 sample, indicating a strong synergistic effect between Zr and Si. The methanol selectivity exhibits a volcano-like behavior with an increasing Zr/(Zr+Si) ratio in supports, reaching its maximum on Cu/ZrSi-35 sample at all three reaction temperatures. A strong effect on Cu from support components could be achieved by regulating Zr/Si ratio in support. Moreover, the physical mixing (PM) of FSP-made Cu/SiO_2 and Cu/ZrO_2 powder with the same composition to SFSP-Cu/ZrSi-35 sample exhibits much lower activity and methanol selectively (Figure S8), demonstrating that a strong Zr-Si interaction is created during FSP preparation after mixing Zr and Si precursors in the liquid phase. The TOF value of Cu/ZrSi-35 is much higher than those samples without Zr (Cu/ZrSi-0) or Si (Cu/ZrSi-100) in Figure 1d, exceeding the single-atom Cu/ZrO_2 catalysts[34] and exhibiting the best methanol yield at a relatively low temperature (Table S3).

Reduction behavior of Cu species

In-situ XAS was used to identify the variations of the Cu valence state during reduction and the evolution of the coordination environment of Zr atoms in the CO_2 atmosphere and during CO_2-hydrogenation in a recently developed high-pressure cell[29]. The as-prepared, reduced and catalysts after reaction were characterized by extended X-ray absorption fine structure (EXAFS), while the dynamic structural evolution during reduction, in CO_2 atmosphere, as well as during reaction at low and high pressures was monitored by X-ray absorption near-edge structure (XANES) spectroscopy. The details of the process and reaction conditions at each step are described in Figure S9.

The change in the oxidation state of Cu has been monitored by *in-situ* XANES at the Cu K-edge up to 300 eV above the edge. In Figure S10, the white line of Cu^{2+} gradually decreases, while the pre-edge feature that occurs due to 1s to 3d electronic transition at 8981 eV assigned to Cu^0 gradually appears with increasing temperatures for all tested samples. These changes in the spectral shape during the heating in H_2

atmosphere indicate the evolution of Cu species, and the component fractions that obtained from the linear combination fitting (LCF) results are plotted in Figures 2(a-d). The Cu K-edge XANES spectra of standard CuO, Cu, Cu_2O and shattuckite are used in LCF, where the fitting errors are controlled in ±5% (Figure S11) according to our previous work[17]. Cu^{2+} in the form of CuO can be reduced stepwise into Cu^+ at a low temperature and then further reduced to Cu^0 with increasing temperature. This stepwise reduction behavior especially occurs if Cu^+ is stabilized[33]. For Cu/ZrSi-0, the amount of CuO is equal to the shattuckite-like species in the as-prepared state. Cu^+ probably stems from the reduction of shattuckite-like species, considering that its consumption is synchronous with the Cu^+ formation and before CuO reduction. Cu^+ fitted as Cu_2O reaches a maximum of 47% when the shattuckite-like Cu is fully consumed. After that the fraction of Cu^+ decreases due to the further reduction to Cu, exhibiting a volcano curve in the temperature range of 140-190 °C and keeps stable at around 20%. When adding a small amount of Zr into SiO_2 support (Cu/ZrSi-3), the initial fraction of shattuckite-like Cu decreases. The variation of the fraction of Cu^+ species also follows a volcano curve with a maximum of about 53% and finally the fraction of Cu^+ stays at 34%. It suggests that the Zr addition is favorable to Cu^+ species formation and inhibits the complete reduction into Cu^0. When further increasing the Zr content in the support (Cu/ZrSi-35), the amount of shattuckite-like Cu species decreases to about 30% in the as-prepared catalyst. The Cu^+ content stops following the volcano trend but stays unchanged once it reaches the maximum (43%). However, it decreases to 22% without the contribution of Si in the Cu/ZrSi-100 sample, indicating that the ratio of Cu^+/Cu^0 can be well regulated by the Zr and Si constituents in the support. From the normalized XANES spectra at the Cu K-edge of reduced samples in Figure 2e, the features are similar to those in metallic Cu reference, but slightly change with different Zr/(Zr+Si) ratios. The FT k^3-weighted EXAFS spectra after TPR (not corrected for the phase shift) are illustrated in Figure 2f. The main backscattering contribution at 2.24 Å can be well observed in all reduced samples, which is assigned to Cu−Cu coordination in metallic Cu. The most significant Cu−O scattering at 1.25 Å (typical for Cu_2O) is detected in Cu/ZrSi-35, which is consistent with the LCF results.

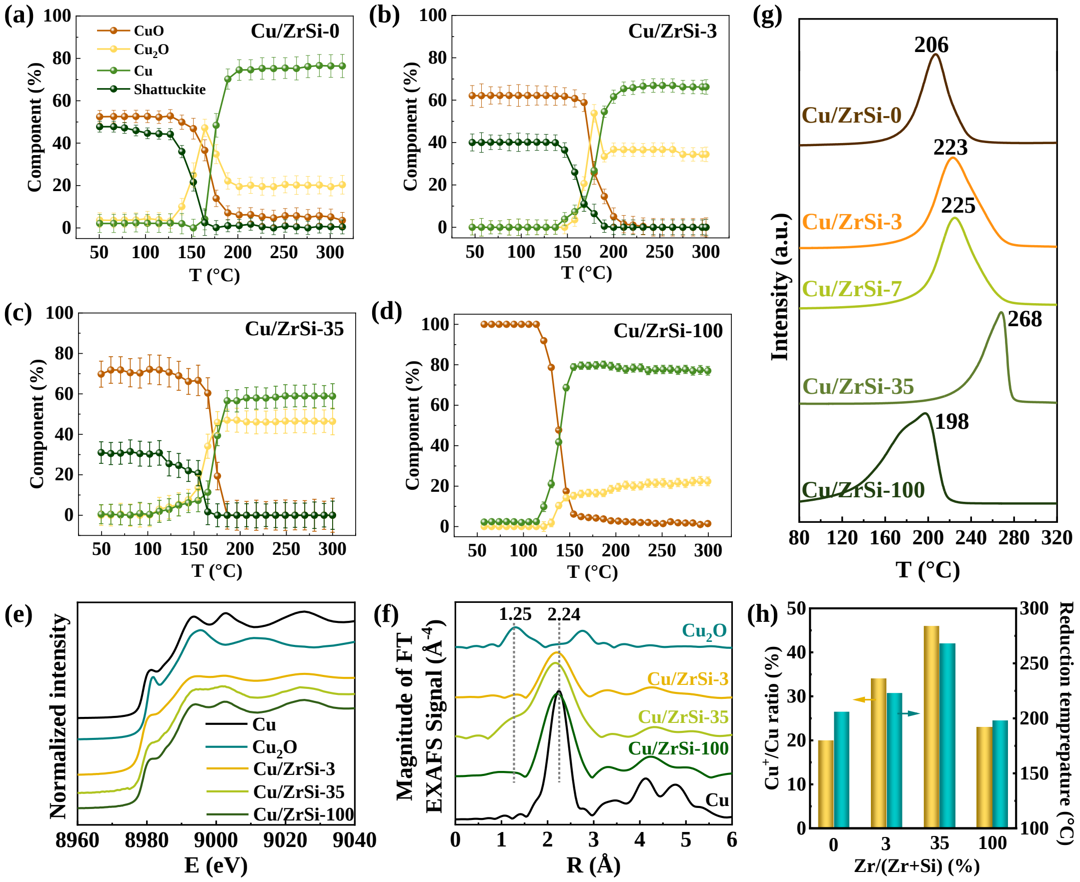

Figure 2. Characterization of Cu species. Variations of Cu species (Cu, Cu_2O, CuO and shattuckite) during TPR over (a) Cu/ZrSi-0, (b) Cu/ZrSi-3, (c) Cu/ZrSi-35 and (d) Cu/ZrSi-100 samples; normalized XANES spectra (e) and k^3-weighted FT EXAFS spectra (f) at Cu K-edge after reduction; (g) H_2-TPR profiles of all catalysts; (h) effect of Zr/(Zr+Si) ratio on the Cu reduction behavior, including Cu reduction temperature during TPR experiments and the Cu^+/Cu^0 ratio determined by XAS.

Temperature-programmed reduction (TPR) was further conducted to investigate the reduction behavior of copper as shown in Figure 2g. The reduction temperature of Cu species varies in the range between 198 and 268 °C dependent on the Zr/(Zr+Si) ratios, revealing that the composition of support greatly affects the reducibility of Cu species due to different interaction strengths between Cu and support[35]. The variations of reduction temperature and Cu^+/Cu^0 ratio determined by LCF at Cu K-edge XANES between 8960 and 9040 eV with Zr/(Zr+Si) ratio are summarized in Figure 2h. Both of them exhibit volcano-like trends with a maximum achieved at the sample with a ratio of 35%. Besides, from the CO-FTIR spectra in Figure S12a, the band at 2125 cm^{-1} that can be assigned to the linear stretching frequency of Cu^+−CO species appears for all Cu-based catalysts, while the Cu^0−CO stretching frequency is mainly observed in the Cu/ZrO_2 sample due to the CO desorption on the Zr-Si oxides supported Cu catalysts at experimental conditions (Figure S12b). A blue shift of the peak is observed for the three Cu-Zr-Si samples, hinting at the formation of a strong bond between CO and Cu^+, which has been proven to be more stable and active compared with the generally-accepted CO−Cu^+ site around 2125 cm^{-1} wavenumber[36].

Identification of Zr species

The evolution of the coordination environment of Zr atoms in the CO_2 atmosphere and during the reaction was monitored by *in-situ* XAS at the Zr K-edge. The typical feature at 18011 eV confirms that the valence state of Zr is +4 for all the tested samples[37] (Figures 3a and 3b). However, the features around the white line become broader and less intense with decreasing Zr content in support compared to the t-ZrO_2 reference. The local structure of Zr varies with the Zr content according to the shape of peaks in the range of 18020 to 18050 eV. From the EXAFS data in Figure 3c, the distance between Zr and O becomes smaller, and the Zr−O−Zr bond is elongated in the Cu/ZrSi samples compared to the t-ZrO_2 reference. The EXAFS features marked with a circle in Figure 3d vary with Zr/(Zr+Si) ratio, confirming the existence of a structural distortion caused by Zr-Si interactions at a longer distance in the Zr species that are always observed during the quenching process in the FSP method[38].

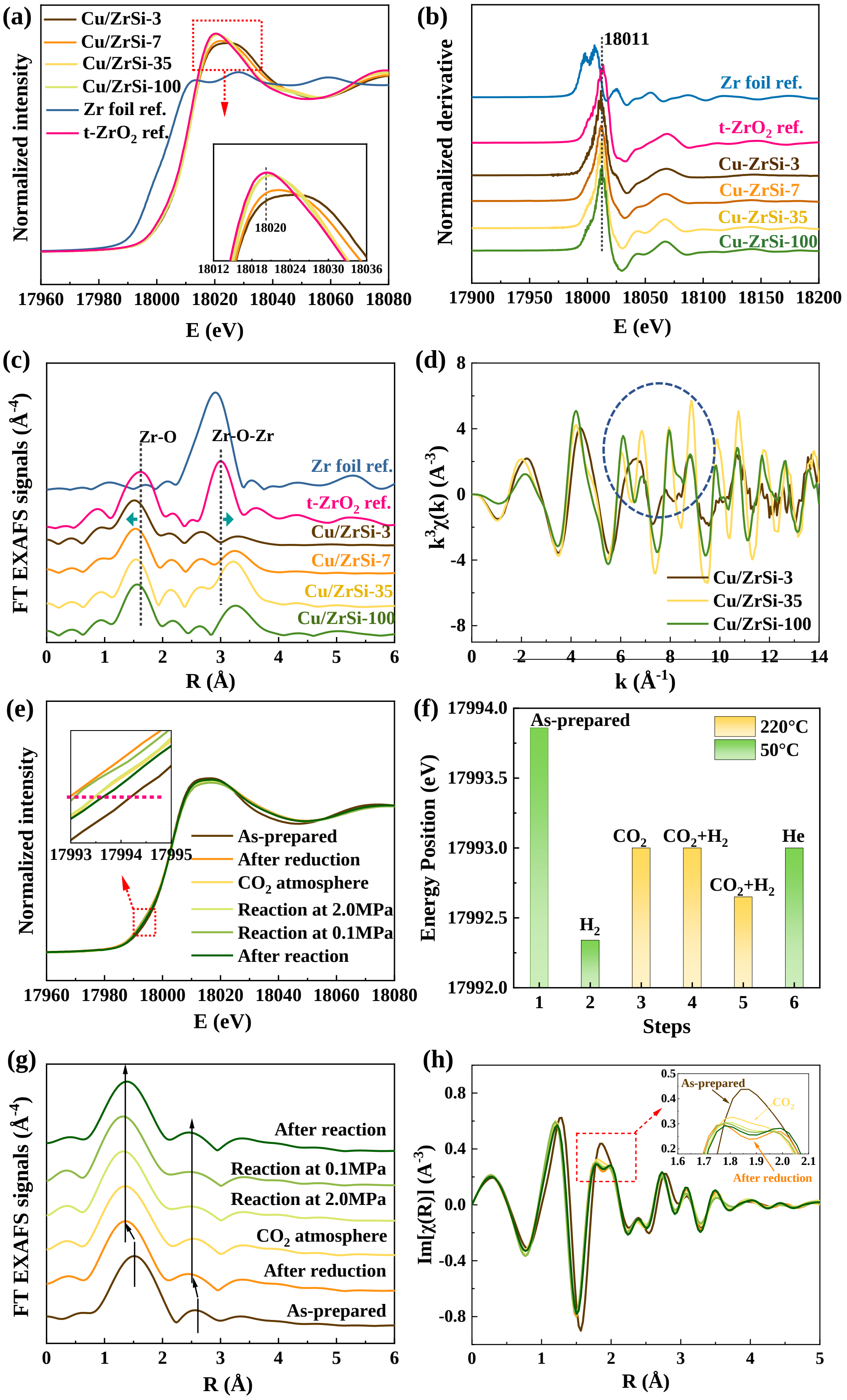

Figure 3. Characterization of Zr species. (a) Normalized XANES spectra; (b) first derivatives of XANES spectra; (c) magnitude of FT k^3-weighted EXAFS spectra; (d)

their k space at Zr K-edge for the series of as-prepared Cu/ZrSi-x samples; Evolution of Zr structure identified by *in-situ* XAS technique: (e) XANES spectra at Zr K-edge of Cu/ZrSi-3 sample measured at the different steps of treatments; (f) Specific energy position of the selected area in the insert of Figure 3e at different treatments; (g) FT k^3-weighted EXAFS spectra at Zr K-edge of Cu/ZrSi-3 measured at the different experimental steps and (h) their imaginary part.

To identify the local structure of Zr species, the EXAFS spectra of as-prepared samples were fitted by using a tetragonal ZrO_2 model with a structure of two Zr−O shells at 2.10 Å (CN=4) and 2.20 Å (CN=4), as well as one Zr−O−Zr shell at 3.54 Å (CN=4)[39]. The EXAFS fitting results of the ZrO_2 reference and each sample are listed in Table 1. The distances of the first Zr−O shell for all samples are around 2.10 Å, while those of the second shell vary with the Zr content. The distance becomes larger from 2.24 to 2.32 Å with the increase of the Zr/(Zr+Si) molar ratio and exhibits a volcano-like trend with a maximum for the Cu/ZrSi-35 sample. The change of the second oxygen subshell around the Zr atoms can be explained by the existence of oxygen displacements perpendicular to the z direction[40]. For the Zr−O−Zr shell, the distances of all samples are larger than that in the reference ZrO_2, hinting at the distorted structure formed during FSP preparation as reported[41]. An increase of CNs from 0.5 to 3.8 and a slight decrease in the distance with the increased Zr/(Zr+Si) ratio are observed. In the Cu/ZrSi-3 sample, the CN of Zr−O−Zr is 0.5, suggesting that ZrO_2 is atomically dispersed in the SiO_2 matrix with pseudo-single-atom structures[42], which can be denoted as Zr_nO_x (n=1 or 2). It confirms that large number of single-site Zr species coexist with small ZrO_2 clusters. In comparison, the CN of Zr−O−Zr in Cu/ZrSi-100 is 3.8, which is close to the bulk ZrO_2, suggesting the ZrO_2 particle size increases with Zr content.

Table 1. Fitting parameters resulting from the analysis of k^3-weighted EXAFS at Zr K-edge collected at 50°C for the as-prepared catalysts. Spectra were fitted in the range of R = 1.0-3.7 Å and k = 3.0-12.0 $Å^{-1}$.*

Samples	Zr−O shell			Zr−O−Zr shell			δE_0/eV	r factor
	CN	R/Å	$\sigma^2/10^{-3}$ $Å^2$	CN	R/Å	$\sigma^2/10^{-3}$ $Å^2$		
t-ZrO_2 ref.	4.1±0.7	2.10±0.02	3.7±2.7	3.9±1.3	3.47±0.02	3.7±2.6	7.7±1.8	0.032
	4.1±0.7	2.20±0.02						
Cu/ZrSi-3	3.5±0.7	2.10±0.02	3.6±2.4	0.5±0.3	3.64±0.02	6.4±3.6	0.8±1.6	0.023
	2.4±0.4	2.24±0.03						
Cu/ZrSi-7	4.4±0.8	2.10±0.02	6.1±2.3	1.4±0.5	3.63±0.01	3.7±2.3	0.7±1.4	0.013
	2.1±0.4	2.29±0.04						
Cu/ZrSi-35	4.7±0.8	2.11±0.01	5.3±1.8	3.1±0.6	3.62±0.01	4.7±1.6	1.4±1.3	0.013
	2.3±0.5	2.32±0.03						
Cu/ZrSi-100	3.8±1.1	2.10±0.02	3.7±2.8	3.8±1.3	3.61±0.02	12.3±3.0	0.6±1.6	0.032
	2.0±0.5	2.28±0.04						

*Note: The amplitude reduction factor (S_0^2) was fixed at 0.95. The coordination numbers (CN), the bond lengths (R) and the Debye-Waller factors (σ^2) were derived as guess parameters. The r factor represents the quality of the fit.

From the detailed fitting spectra (Figure S13), the Zr−O shell at about 1.6 Å and the Zr−O−Zr shell at 3.2 Å (without phase correction) can be well fitted for Cu/ZrSi-3 and Cu/ZrSi-7 samples, but the fitting is slightly unmatched in the distance ranging from 2.2 to 3.0 Å. For comparison, the structure of ZrO_2 in Cu/ZrSi-35 and Cu/ZrSi-100 samples can be well-fitted, revealing that the coordination environment of Zr atoms is possibly affected by SiO_2 through the formation of Zr−O−Si bonds, especially in the samples with a little amount of Zr. A distinguished structure (Zr−O−Si) between Zr−O and Zr−O−Zr shells is established during the FSP process due to the strong Zr-Si interaction, further confirming the single-site Zr species in the SiO_2 matrix. Note that these species cannot be excluded in Cu/ZrSi-35 sample, although they are not directly observed, because the EXAFS signals present the average coordination of Zr atoms. Some information on Zr-Si interaction might be covered by the existence of a large amount of bulk ZrO_2 with an increase in the Zr/(Zr+Si) ratio. Besides, the white line of reacted samples in the Zr K-edge XANES data shows the same trend as the fresh ones (Figure S14a), and the shift of Zr−Zr distance can be observed in all reacted Cu/ZrSi-x samples (Figure S14b), suggesting that the structure of Zr species remains stable during the reaction.

Considering the limitation of the XAS technique on determining surface species, the Zr-Si species were additionally characterized by X-ray photoelectron spectroscopy (XPS, see Figure S15). Peaks at 103.5 and 102.7 eV in the Si 2*p* XPS spectra can be assigned to SiO_2 and SiO_x, respectively[43]. A new peak belonging to $ZrSiO_4$ species at 102.0 eV[44] appeared only on the catalysts supported by Zr-Si oxides. The proportion of this peak gradually increases from 7.2 to 18.2 % with increasing Zr content from 3 to 35% due to the strengthened Zr-Si interaction. It also confirms the existence of single-site Zr in all Cu/Zr-Si catalysts, which are stabilized by SiO_2 through Zr−O−Si coordinates.

Dynamic variations of Zr species

The variations of the Zr coordination sphere of Cu/ZrSi-3 sample at different conditions, namely in CO_2 atmosphere at high pressure (2.0 MPa) and in CO_2+H_2 reaction at both high (2.0 MPa) and low (0.1 MPa) pressures, were successively monitored by *in-situ* XANES at Zr K-edge. The XANES spectra (Figure 3e) do not show any obvious changes in the white line features during the whole process, confirming the stability of the atomically dispersed Zr in the SiO_2 matrix. However, energy shifts can be detected at the edge (given in the insert). The energy position in the edge is plotted with the sequences of the steps in Figure 3f. It shifts to lower energy after reduction and back to higher energy in the CO_2 atmosphere at 2.0 MPa, revealing that Zr oxide can be slightly reduced in H_2 at 300°C and oxidized in CO_2 at 230°C. Further introducing hydrogen at the same pressure does not change the energy position of the edge, consequently exhibiting a low structure sensitivity to hydrogen in the presence of CO_2. The energy down-shift is detected when the pressure is released, which is caused by less adsorption of intermediates at 0.1 MPa. After the He purge, the energy is still less than that at the initial state, suggesting that the Zr valence state is irreversibly changed during the whole process. It is affected by the atmosphere, pressure and temperatures. Partially reduced ZrO_{2-x} is proposed to facilitate the methanol formation by activating the key reaction intermediates[9].

The FT EXAFS spectra in the R space and their imaginary part of each step are shown in Figures 3g and 3h, respectively. The most obvious variation can be observed after reduction, exhibiting obvious shifts corresponding to the Zr−O and Zr−O−Zr bonds and distinct features at a longer distance compared to those at the following steps. The variations in different atmospheres and pressures are clearly seen in the imaginary part of R space. Especially at R-values of 1.6 to 2.1 Å, the oxidized Zr species exhibit one peak, while reduction leads to a peak split. The reduced Zr species can be partially re-oxidized in the CO_2 atmosphere but will not return to the initial state. We propose that the observed Zr site with an unsaturated local coordination structure is sensitive to reaction conditions and might be essential to activate CO_2 and promote its transformation, verifying the Zr component is effective in improving catalytic performances[45]. Unfortunately, this distorted structure and variations are not observed in Cu/ZrSi-35 from either the pre-edge of Zr K-edge XANES or the FT EXAFS spectra at different conditions as shown in Figure S16. That is because the symmetry of Zr coordination is only sensitive to the very surface[46], and the signal will be covered by the stable state in bulk in Cu/ZrSi-35 sample.

Analysis of reaction pathways

It has been widely accepted that CO_2 hydrogenation to methanol over Cu-based catalysts follows two major reaction pathways[9]. One is featured by the CO* intermediate that is produced from the reverse water-gas-shift (RWGS: $CO_2 + H_2 \rightarrow CO + H_2O$) reaction, which is denoted as the RWGS+CO-hydro pathway. Here, the adsorbed CO* intermediate will be further hydrogenated into monodentate formate (m-HCOO*, also called carboxylate)[35]. The other pathway is called the formate pathway, where CO_2 is activated and directly transform into bidentate formate (bi-HCOO*). The produced m-HCOO* and bi-HCOO* are finally hydrogenated into methoxy (CH_3O*) and methanol[47]. In general, hydrogen adsorption and dissociation occur mainly on metallic Cu sites, while active species on support are responsible for CO_2 activation. Therefore, the RWGS+CO-hydro pathway mainly occurs on the Cu catalyst with inert SiO_2 support, while the formate pathway is always observed on Cu/ZrO_2 catalyst. From the above analysis, the reaction pathway is strongly affected by the support components due to their distinct activity on the adsorption and conversion of intermediates[48].

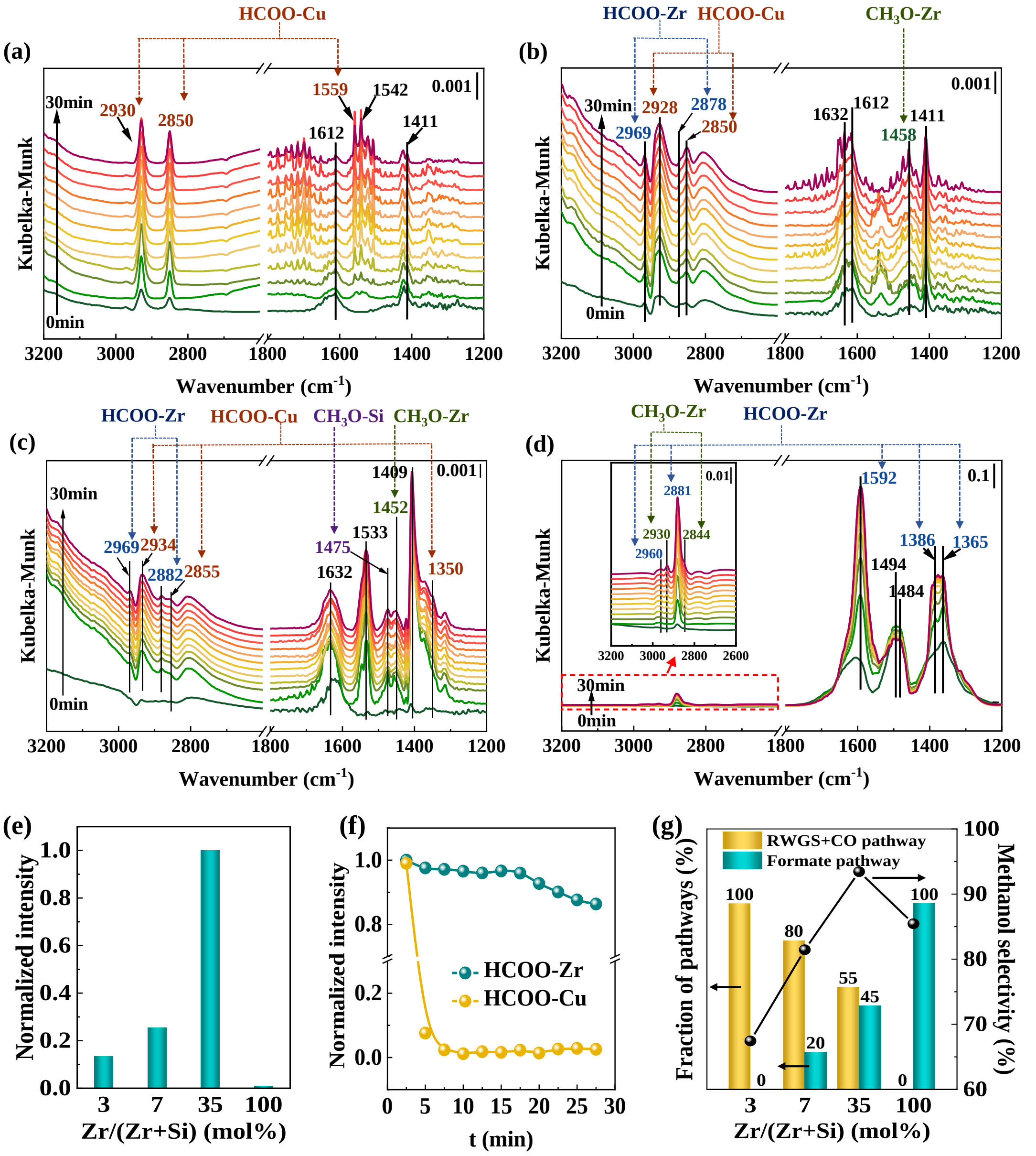

Figure 4. Analysis of intermediates during reaction. *In-situ* DRIFT spectra of (a) Cu/ZrSi-3, (b) Cu/ZrSi-7, (c) Cu/ZrSi-35 and (d) Cu/ZrSi-100 samples during CO_2

hydrogenation reaction (CO_2:H_2=1:3) at 0.1 MPa and 230 °C with a flow rate of 20 mL/min. Analysis of the results of DRIFTS: (e) peak intensity of CO_3^{2-}-Cu in DRIFT spectra of a series of Cu/ZrSi-x samples normalized by that in Cu/ZrSi-35; (f) the evolution of normalized peak area of HCOO-Cu (2850 cm^{-1}) in Cu/ZrSi-3 and HCOO-Zr (2882 cm^{-1}) in Cu/ZrSi-100 with the time of He sweep; (g) the fraction of reaction pathways and their contributions to methanol selectivity over Cu/ZrSi-x samples with various Zr/(Zr+Si) ratios.

In Figure 4, the evolution of the key intermediates and the specific adsorption sites for each reduced catalyst was monitored by *in-situ* DRIFTS, and representative intermediates are especially analyzed to clearly understand the additive effect of the two reaction pathways. Details of infrared band assignments of the surface species are listed in Table S4. Formate species are not specified in this work due to easily overlapped infrared bands of bi-HCOO* and m-HCOO*[9], but their adsorption site is distinguishable and significant to intermediates transformation during the whole process. Carbonaceous species, such as bicarbonate or carbonate ion with features at 1632-1409 cm^{-1}, are sensitive to Cu and Zr adsorption sites on SiO_2-containing catalysts in Figures 4(a-c). The adsorption of CO_3^{2-}-Cu[49] at 1409-1411 cm^{-1} is strengthened with an increase of the Zr/(Zr+Si) ratio, reaching the maximum at Cu/ZrSi-35 in the series of Cu/ZrSi-x catalysts as illustrated in Figure 4e, which is related to the variations of Cu^+ content. Cu^+ species on Cu/SiO_2-containing catalysts seem to be responsible for intensifying the CO* adsorption and conversion to promote hydrogenation reaction to methanol from our previous work[17]. HCO_3^--Cu at 1632 cm^{-1} is identified in Cu/ZrSi-7 and intensified in Cu/ZrSi-35. HCO_3^--Zr (1617-1612 cm^{-1}) can be observed only at a low ratio of Zr/(Zr+Si) in Cu/ZrSi-3 and Cu/ZrSi-7 samples, while CO_3^{2-}-Zr (1533 cm^{-1}) with strong intensity is stabilized in Cu/ZrSi-35, which can be attributed to the disordered ZrO_2 structure with oxygen vacancy as reported to be active in methanol production[50]. Furthermore, the adsorption of formate on Cu (HCOO-Cu, at 2930, 2850, 1559 and 1350 cm^{-1})[48] and Zr (HCOO-Zr, at 2969, 2875-2882, 1592, 1365 cm^{-1})[9] both get stronger with increasing Zr/(Zr+Si) ratio for those with combined Zr and Si support, verifying that carbonaceous species are hydrogenated into formate on both Cu and Zr sites. Bands of methoxy (at 1475 and 1458-1452 cm^{-1}) are identified in Cu/ZrSi-35 from Figure 4c, indicating that the hydrogenation of formate to methoxy is intensified. In contrast, for Cu/ZrSi-100 in Figure 4d, carbonaceous species or adsorption on Cu sites cannot be observed. Instead, the intensity of HCOO-Zr at 1592, 1386 and 1365 cm^{-1} is ten times higher than those in SiO_2-supported catalysts, indicating that a large number of carbonaceous species are hydrogenated into formate on ZrO_2 support. The adsorption strength of formate species can be characterized by the desorption of HCOO-Cu and HCOO-Zr intermediates during the He purge as shown in Figure S17. HCOO-Cu at 2850 cm^{-1} can be easily swept away from the surface, while HCOO-Zr signals keeps stable as plotted in Figure 4f, leading to the strong adsorption and weak transformation of intermediates on Zr active sites. The accumulation of formate species on ZrO_2 support will lead to a decrease of activity for further hydrogenation in the formate pathway[51], resulting in the lower methanol production observed for Cu/ZrSi-100 compared to that for Cu/ZrSi-35. Consequently, the sequential activation of reactants and the conversion of intermediates are essential for the tandem hydrogenation reactions, which is able to be controlled by the regulation of support components *via* the combined RWGS+CO-hydro and formate pathways. The formate species on Cu and Zr sites (denoted as HCOO-Cu and HCOO-Zr) can be treated as markers for RWGS+CO-hydro and formate reaction pathways, respectively, from the comparison between the SiO_2 dominated Cu/ZrSi-3 and the ZrO_2 dominated Cu/ZrSi-100 samples. The RWGS+CO-hydro pathway is partially replaced by the formate pathway with the increase of Zr(Zr+Si) ratio as indicated in Figure 4g, confirming the shift between the two reaction pathways induced by the enhanced Zr-Si synergy. Both of them are beneficial for converting carbonaceous species into formate during methanol synthesis and they will contribute most to methanol selectivity when the proportion of the two pathways is nearly equal.

It is worth to note that none of the observed reaction pathways are consistent with the variations of Cu^+ species. It demonstrates that Cu^+ species may relate to the CO_2 activation by polarizing the C=O bond, and the coexisted Cu^0 is beneficial to H_2

dissociation[52], while the structure of Zr species determines the following hydrogenation process and products distribution.

Analysis of reaction mechanism

DFT calculations were conducted to obtain molecular insights into the reaction pathways on different Zr sites. Two Cu/SiO_2 models with single-site Zr (Model 1, denoted as Cu/Zr_1-Si) and ZrO_2 nanoparticles (Model 2, denoted as Cu/ZrO_2-Si) and their potential interfacial active sites were established. Figure 5 (a-f) shows DFT-optimized geometries of CO_2 adsorption on different sites, such as the Cu-Zr interface, Cu surface and Zr species, in each model. CO_2 adsorption energy on different sites that were used to determine the possibility of CO_2 desorption was calculated using VASP. In Model 1, the adsorption of CO_2 is weak on both the Cu surface and single-site Zr with the adsorption energy of −0.28 and −0.90 eV, respectively, whereas the bridged adsorption on Cu-Zr_1 interface with the carbon atom bound to the Cu surface and one oxygen atom interact with Zr_1 is strong (−1.95 eV). However, the bridged CO_2 adsorption on the Cu-ZrO_2 interface in Model 2 is unstable, where a stable adsorption structure is unavailable after optimization as shown in Figure S18. The most stable structure for Model 2 is CO_2 adsorption on ZrO_2 with an adsorption energy of −0.34 eV. Therefore, we found a much more favorable adsorption mode of CO_2 at the interface between Cu and single-site Zr, revealing that the CO_2 adsorption and activation are prior on single-site Zr rather than ZrO_2 nanoparticles when they coexist in Cu-based catalysts. After CO_2 adsorption, the mode of $^*CO_2$ hydrogenation determines the reaction pathways in the subsequent hydrogenation processes. The hydrogenation could occur on the terminal O of bridged CO_2 adsorption mode to form HOCO* intermediate (Figures S19-20) or on the terminal C of the structure with two O atoms interacting with two Zr^{4+} Lewis acidic centers of the ZrO_2 surface to form HCOO* intermediate, following RWGS+CO-Hydro and formate pathway, respectively[9,13]. The relative energy of transition states (TS) of the two pathways is compared to determine the most favorable pathway on each Model, as presented in Figure 5(g). The $^*CO_2$ can only be hydrogenated to *HOCO due to the lack of the essential two Zr^{4+} Lewis acidic centers on the Cu/Zr$_1$-Si surface, while it is more facile to *HCOO than that to *HOCO on Cu/ZrO$_2$-Si. It suggests that the RWGS+CO-Hydro pathway can be strengthened by the single-site Zr, while the ZrO$_2$ particles are responsible for the promotion of the formate pathway. The above analysis accords well with the phenomenon that the dominant pathway changes from RWGS+CO-Hydro to formate with increasing Zr content from the DRIFTS results.

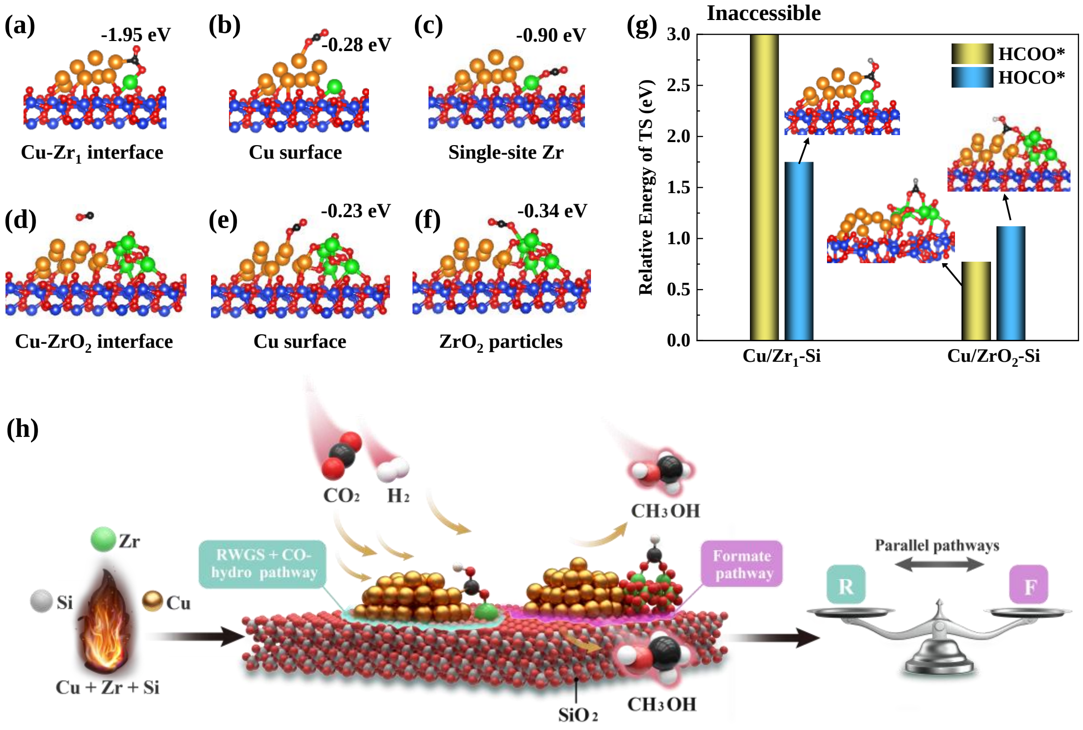

Figure 5. Mechanism analysis. DFT optimized geometries of CO$_2$ adsorption on different sites of Cu/Zr-Si catalysts and their adsorption energies (marked nearby each structure): Cu-Zr interface (a and d), Cu surface (b and e) and Zr species (e and f), where the upper ones (a, b and c) belong to Model 1 with single-site Zr, and the bottom ones (d, e and f) belong to Model 2 with ZrO$_2$ nanoparticles on Cu/SiO$_2$ catalysts. (g) The relative energy of transition states (TS) on Model 1 (Cu/Zr$_1$-Si) and Model 2 (Cu/ZrO$_2$-Si) during the hydrogenation process to intermediates HCOO* and HOCO*, which follow formate and RWGS+CO-hydro pathways, respectively. Cu: orange, Zr: green; Si: blue, O: red, C: black, and H: gray. (h) Schematic diagram of the parallel reaction pathways on single-site Zr and ZrO$_2$ nanoparticles of Cu/Zr-Si catalysts for methanol synthesis from CO$_2$ hydrogenation.

As shown in Figure 5h, a facile synthesis of single-site Zr in the SiO_2 matrix is achieved by introducing all Cu, Zr and Si precursors into a single flame. The CO_2 is prior to adsorb on the single Zr sites through a bridged adsorption mode with the C atom bound to Cu and one O atom interact with the single Zr atom, forming HOCO* intermediates and hydrogenating in RWGS+CO-hydro pathway. The CO_2 adsorption on ZrO_2 nanoparticles is more favorite in the mode of two O atoms of CO_2 connecting with duel Zr sites. The formed HCOO* intermediates will be hydrogenated following the formate pathway. The coexistence of single-site Zr and ZrO_2 will promote two parallel pathways and maximize the methanol production when they are balanced.

Conclusion

The effect of multi-component support (ZrO_2-SiO_2) on Cu catalysts for CO_2 hydrogenation to methanol has been investigated, uncovering a strong Zr-Si synergy. Both the catalytic activity and the Cu^+ species are observed to follow a volcano-like trend as a function of the Zr/(Zr+Si) molar ratio in single-flame-made Cu-Zr-Si ternary catalysts, reaching a maximum at about 0.35. The *operando* XAS results show that single-site Zr species are stabilized in the SiO_2 matrix, where the local coordination environment of Zr atoms is sensitive to the reaction conditions. DFT calculation reveals that the CO_2 molecules preferentially adsorb on the interface of Cu and single-site Zr in a bridge mode and hydrogenate in RWGS+CO-hydro pathway, while the formate pathway dominates on ZrO_2 nanoparticles. The *in-situ* DRIFT experiments confirm that the creation of single-site Zr in SiO_2 support expands the parallel RWGS+CO-hydro pathway that is always disadvantageous on ZrO_2 support compared to the formate pathway. Thus, methanol productivity is greatly enhanced by maximize Cu^+ species for CO_2 activation and expanding a pathway for intermediate conversion. The present work supplies a feasible strategy for creating a new active site (atomically dispersed oxides) and unlocking a dual-channel pathway to enhance the efficiency of methanol synthesis.

Acknowledgments

This study was supported by the Natural Science Foundation of China (Grant 22172169) and the SPP2080 project (GR 3987/14-1). We would like to thank the Institute for Beam Physics and Technology (IBPT-KIT) for the operation of the storage ring at the Karlsruhe Research Accelerator (KARA). We acknowledge the KIT Light Source for the provision of beamtime and the instruments at the CAT-ACT beamline. Dr. Yu greatly acknowledges the visiting scholarship supported by the Chinese Academy of Sciences (CAS).

Reference

1. Shih, C.F. et al. Powering the Future with Liquid Sunshine. *Joule* **2**, 1925-1949 (2018).
2. Marlin, D.S. et al. Process Advantages of Direct CO_2 to Methanol Synthesis. *Front. Chem.* **6**, 446-454 (2018).
3. Porosoff, M.D. et al. Catalytic reduction of CO_2 by H_2 for synthesis of CO, methanol and hydrocarbons: challenges and opportunities. *Energy Environ. Sci.* **9**, 62-73 (2016).
4. Ahmad, K. & Upadhyayula, S. Greenhouse gas CO_2 hydrogenation to fuels: A thermodynamic analysis. *Environ. Prog. Sustainable Energy* **38**, 98-111 (2019).
5. Ruland, H. et al. CO_2 Hydrogenation with $Cu/ZnO/Al_2O_3$: A Benchmark Study. *ChemCatChem* **12**, 3216-3222 (2020).
6. De, S. et al. Advances in the Design of Heterogeneous Catalysts and Thermocatalytic Processes for CO_2 Utilization. *ACS Catal.* **10**, 14147-14185 (2020).
7. Zhong, J. et al. State of the art and perspectives in heterogeneous catalysis of CO_2 hydrogenation to methanol. *Chem. Soc. Rev.* **49**, 1385-1413 (2021).
8. Pandit, L. et al. Unravelling the Zn-Cu Interaction during Activation of a Zn-promoted Cu/MgO Model Methanol Catalyst. *ChemCatChem* **13**, 4120-4132

(2021).

9. Kattel, S. et al. Optimizing Binding Energies of Key Intermediates for CO_2 Hydrogenation to Methanol over Oxide-Supported Copper. *J. Am. Chem. Soc.* **138**, 12440-12450 (2016).
10. Noh, G. et al. Lewis Acid Strength of Interfacial Metal Sites Drives CH_3OH Selectivity and Formation Rates on Cu-Based CO_2 Hydrogenation Catalysts. *Angew. Chem., Int. Ed.* **60**, 9650-9659 (2021).
11. Yang, M. et al. Flame-made Cu/ZrO_2 catalysts with metastable phase and strengthened interactions for CO_2 hydrogenation to methanol. *Chem. Commun.* **57**, 7509-7512 (2021).
12. Tada, S. et al. Design of Interfacial Sites between Cu and Amorphous ZrO_2 Dedicated to CO_2-to-Methanol Hydrogenation. *ACS Catal.* **8**, 7809-7819 (2018).
13. Larmier, K. et al. CO_2-to-Methanol Hydrogenation on Zirconia-Supported Copper Nanoparticles: Reaction Intermediates and the Role of the Metal–Support Interface. *Angew. Chem. Int. Ed.* **56**, 2318-2323 (2017).
14. Ro, I. et al. Role of the Cu-ZrO2 Interfacial Sites for Conversion of Ethanol to Ethyl Acetate and Synthesis of Methanol from CO2 and H2. *ACS Catal.* **6**, 7040-7050 (2016).
15. Liu, T. et al. In Situ Generation of the Cu@3D-ZrO_x Framework Catalyst for Selective Methanol Synthesis from CO_2/H_2. *ACS Catal.* **10**, 93-102 (2020).
16. Li, K. & Chen, J. CO_2 Hydrogenation to Methanol over ZrO_2-Containing Catalysts: Insights into ZrO_2 Induced Synergy. *ACS Catal.* **9**, 7840-7861 (2019).
17. Yu, J. et al. Stabilizing Cu^+ in Cu/SiO_2 Catalysts with a Shattuckite-Like Structure Boosts CO_2 Hydrogenation into Methanol. *ACS Catal.* **10**, 14694-14706 (2020).
18. Wang, L. et al. Silica accelerates the selective hydrogenation of CO_2 to methanol on cobalt catalysts. *Nat. Commun.* **11**, 1033 (2020).
19. Noh, G. et al. Selective Hydrogenation of CO_2 to CH_3OH on Supported Cu Nanoparticles Promoted by Isolated Ti^{IV} Surface Sites on SiO_2. *ChemSusChem* **12**, 968-972 (2019).

20. Lam, E. et al. Isolated Zr Surface Sites on Silica Promote Hydrogenation of CO_2 to CH_3OH in Supported Cu Catalysts. *J. Am. Chem. Soc.* **140**, 10530-10535 (2018).

21. Liu, X. et al. In Situ Spectroscopic Characterization and Theoretical Calculations Identify Partially Reduced ZnO1−x/Cu Interfaces for Methanol Synthesis from CO2. *Angew. Chem. Int. Ed.* **61**, e202202330 (2022).

22. Dalebout, R. et al. Insight into the Nature of the ZnOx Promoter during Methanol Synthesis. *ACS Catal.* **12**, 6628-6639 (2022).

23. Beck, A. et al. Following the structure of copper-zinc-alumina across the pressure gap in carbon dioxide hydrogenation. *Nature Catal.* **4**, 488-497 (2021).

24. Yang, M. et al. Probing the Nature of Zinc in Copper-Zinc-Zirconium Catalysts by Operando Spectroscopies for CO2 Hydrogenation to Methanol. *Angew. Chem. Int. Ed.* **62**, e202216803 (2023).

25. Yang, M. et al. Flame-made Cu/ZrO_2 catalysts with metastable phase and strengthened interactions for CO_2 hydrogenation to methanol. *Chem. Commun.* **57**, 7509-7512 (2021).

26. Tada, S. et al. Flame spray pyrolysis makes highly loaded Cu nanoparticles on ZrO_2 for CO_2-to-methanol hydrogenation. *Chem. Eng. J.* **381**, 122750-122761 (2020).

27. Kammler, H.K. et al. Flame Synthesis of Nanoparticles. *Chemical Engineering & Technology* **24**, 583-596 (2001).

28. Sarma, B.B. et al. Design of Single-Atom Catalysts and Tracking Their Fate Using Operando and Advanced X-ray Spectroscopic Tools. *Chem. Rev.* (2022).

29. Pandit, L. et al. Versatile in situ/operando Setup for Studying Catalysts by X-Ray Absorption Spectroscopy under Demanding and Dynamic Reaction Conditions for Energy Storage and Conversion. *Chemistry–Methods* **2**, e202100078 (2022).

30. Koirala, R. et al. Synthesis of catalytic materials in flames: opportunities and challenges. *Chem. Soc. Rev.* **45**, 3053-3068 (2016).

31. Yang, M. et al. Probing the Nature of Zinc in Copper-Zinc-Zirconium Catalysts

by Operando Spectroscopies for CO_2 Hydrogenation to Methanol. *Angew. Chem. Int. Ed.*, e202216803 (2023).

32. Pokhrel, S. et al. Custom-Designed Nanomaterial Libraries for Testing Metal Oxide Toxicity. *Acc. Chem. Res.* **46**, 632-641 (2013).
33. Dong, X. et al. Comparative study of silica-supported copper catalysts prepared by different methods: formation and transition of copper phyllosilicate. *Catal. Sci. Technol.* **6**, 4151-4158 (2016).
34. Zhao, H. et al. The role of Cu_1–O_3 species in single-atom Cu/ZrO_2 catalyst for CO_2 hydrogenation. *Nature Catal.* **5**, 818-831 (2022).
35. Wang, W. et al. Probing into the multifunctional role of copper species and reaction pathway on copper-cerium-zirconium catalysts for CO_2 hydrogenation to methanol using high pressure in situ DRIFTS. *J. Catal.* **382**, 129-140 (2020).
36. Zhou, H. et al. Engineering the Cu/Mo_2CT_x (MXene) interface to drive CO_2 hydrogenation to methanol. *Nature Catal.* **4**, 860-871 (2021).
37. Lam, E. et al. Isolated Zr Surface Sites on Silica Promote Hydrogenation of CO_2 to CH_3OH in Supported Cu Catalysts. *J. Am. Chem. Soc.* **140**, 10530-10535 (2018).
38. Liu, S. et al. Fundamentals and recent applications of catalyst synthesis using flame aerosol technology. *Chem. Eng. J.* **405**, 126958 (2021).
39. Salusso, D. et al. Combining X-ray Diffraction and X-ray Absorption Spectroscopy to Unveil Zn Local Environment in Zn-Doped ZrO_2 Catalysts. *J. Phys. Chem. C* **125**, 22249-22261 (2021).
40. Acuña, L.M. et al. Local atomic structure in tetragonal pure ZrO_2 nanopowders. *J. Appl. Crystallogr.* **43**, 227-236 (2010).
41. Zhang, Z. et al. Tailored metastable Ce-Zr oxides with highly distorted lattice oxygen for accelerating redox cycles. *Chem. Sci.* **9**, 3386-3394 (2018).
42. Wei, H. et al. FeOx-supported platinum single-atom and pseudo-single-atom catalysts for chemoselective hydrogenation of functionalized nitroarenes. *Nat. Commun.* **5**, 5634 (2014).
43. Li, H.F. et al. XPS analysis of SiO_2/SiC interface annealed in nitric oxide

ambient. in *SILICON CARBIDE AND RELATED MATERIALS - 1999 PTS, 1 & 2*, Vol. 338-3 (eds. Carter, C.H., Devaty, R.P. & Rohrer, G.S.) 399-402 (2000).

44. Guittet, M.J. et al. Bonding and XPS chemical shifts in $ZrSiO_4$ versus SiO_2 and ZrO_2: Charge transfer and electrostatic effects. *Phys. Rev. B* **63**(2001).

45. Wang, J. et al. A highly selective and stable ZnO-ZrO_2 solid solution catalyst for CO_2 hydrogenation to methanol. *Sci. Adv.* **3**, e1701290 (2017).

46. Docherty, S.R. & Coperet, C. Deciphering Metal-Oxide and Metal-Metal Interplay via Surface Organometallic Chemistry: A Case Study with CO_2 Hydrogenation to Methanol. *J. Am. Chem. Soc.* **143**, 6767-6780 (2021).

47. Wang, Y. et al. Strong Evidence of the Role of H_2O in Affecting Methanol Selectivity from CO_2 Hydrogenation over Cu-ZnO-ZrO_2. *Chem* **6**, 419-430 (2020).

48. Bando, K.K. et al. In-situ FT-IR study on CO_2 hydrogenation over Cu catalysts supported on SiO_2, $A1_2O_3$, and TiO_2. *Appl. Catal. A: Gen.* **165**, 391-409 (1997).

49. Fisher, I.A. & Bell, A.T. In Situ Infrared Study of Methanol Synthesis from H_2/CO over Cu/SiO_2 and Cu/ZrO_2/SiO_2. *J. Catal.* **178**, 153-173 (1998).

50. Pinheiro Araújo, T. et al. Flame-made ternary Pd-In_2O_3-ZrO_2 catalyst with enhanced oxygen vacancy generation for CO_2 hydrogenation to methanol. *Nat. Commun.* **13**, 5610 (2022).

51. Wu, W. et al. CO_2 Hydrogenation over Copper/ZnO Single-Atom Catalysts: Water-Promoted Transient Synthesis of Methanol. *Angew. Chem. Int. Ed.* **61**, e202213024 (2022).

52. Gong, J. et al. Synthesis of Ethanol via Syngas on Cu/SiO_2 Catalysts with Balanced Cu^0–Cu^+ Sites. *J. Am. Chem. Soc.* **134**, 13922-13925 (2012).